Article

Comparison of Perimeter Delineation Methods for Remote Sensing Fire Spot Data in Near/Ultra-Real-Time Applications

Hanif Bhuian [1,†], Hatef Dastour [1,†], Mohammad Razu Ahmed [2] and Quazi K. Hassan [1,*]

1   Department of Geomatics Engineering, University of Calgary, 2500 University Drive NW, Calgary, AB T2N 1N4, Canada
2   Western Arctic Centre for Geomatics, Government of Northwest Territories, Inuvik, NT X0E 0T0, Canada
*   Correspondence: qhassan@ucalgary.ca
†   These authors contributed equally to this work.

Abstract: Forest fires cause extensive damage to ecosystems, biodiversity, and human property, posing significant challenges for emergency response and resource management. The accurate and timely delineation of forest fire perimeters is crucial for mitigating these impacts. In this study, methods for delineating forest fire perimeters using near-real-time (NRT) remote sensing data are evaluated. Specifically, the performance of various algorithms—buffer, concave, convex, and combination methods—using VIIRS and MODIS datasets is assessed. It was found that increasing concave α values improves the matching percentage with reference areas but also increases the commission error (CE), indicating overestimation. The results demonstrate that combination methods generally achieve higher matching percentages, but also higher CEs. These findings highlight the trade-off between improved perimeter accuracy and the risk of overestimation. The insights gained are significant for optimizing sensor data alignment techniques, thereby enhancing rapid response, resource allocation, and evacuation planning in fire management. This research is the first to employ multiple algorithms in both individual and synergistic approaches with NRT or ultra-real-time (URT) active fire data, providing a critical foundation for future studies aimed at improving the accuracy and timeliness of forest fire perimeter assessments. Such advancements are essential for effective disaster management and mitigation strategies.

Keywords: thermal anomaly data; satellite imagery; VIIRS; MODIS; concave α values; matching percentage; commission error; buffer method; convex method

1. Introduction

Forest fires cause widespread destruction to natural ecosystems, human life, and property globally. Recent data indicate that forest fires now result in an average of three million more hectares of tree cover loss per year compared to 2001, accounting for over one-quarter of all tree cover loss over the past two decades [1]. Annually, an average of more than 420 million hectares (Mha) of forest are burned globally [2,3], and the frequency and intensity of these fires have been increasing in recent times [4,5]. The escalation in both the frequency and intensity of these fires is alarming, with climate change, and particularly global warming, playing a significant role [6,7]. However, human activities also contribute substantially to this destruction [6,7]. The economic toll is staggering, with an average annual loss of USD 2.4 billion between 2002 and 2011 [8]. Significant carbon emissions are another concern; for instance, the 1997 Indonesian wildfires released approximately 13–40% of average annual global carbon emissions [9]. The health implications are equally concerning, with smoke from fires exacerbating respiratory and cardiovascular conditions, leading to coughing, breathing difficulties, and eye irritation [10]. Moreover, the human cost is profound, with large fires resulting in numerous fatalities, including to firefighters. For instance, between 1994 and 2004, the United States saw 1144 firefighters lose their

lives in the line of duty [11]. The 2011 Slave Lake fire in Alberta, Canada, serves as a stark reminder of the potential for extensive damage to human settlements, with 40% of the town destroyed, including 454 homes and key municipal buildings, culminating in costs upwards of CAD 700 million [12,13].

In Canada, the trend of increasing forest fire occurrences is a pressing concern [6]. The Canadian Interagency Forest Fire Centre (CIFFC) reported a record-breaking year in 2023, with approximately 17.2 million hectares of forest affected by 7131 fire events, surpassing the previous record set in 1989 [14]. In the same year, Alberta experienced about 2.22 million hectares of forest fires, while the Northwest Territories faced an even larger area of 4.16 million hectares [14]. Given the severity and extent of the damage, it is crucial to accurately measure and monitor forest fire locations and sizes [7,15]. However, the timeliness of official data, such as fire perimeter polygons, remains a challenge, as they are typically made publicly available by the government only at the end of the year or before the onset of the subsequent fire season [16]. This delay hinders early preparation and mitigation efforts, underscoring the need for more research into assessing active forest fire perimeters to enhance fire management and reduce the hazards and severity of forest fires [17].

The advent of Earth Observation (EO) technology has revolutionized the ability to monitor the Earth, offering data from coarse to high spatial resolution and rapid temporal frequency [15]. Active fire products, which detect thermal anomalies, are a critical component of this technology. They serve operational needs such as rapid responses, resource allocation, and evacuation, aiding fire management and firefighting agencies in managing and mitigating the impacts of active forest fires [18,19]. Recent advancements have significantly reduced data latency, providing both global and regional coverage, particularly for the United States and Canada [19]. These active fire products are categorized based on their latency into ultra real-time (URT), real-time (RT), and near real-time (NRT) [20]. The National Aeronautics and Space Administration's (NASA) Earth Observing System Data and Information System (EOSDIS) defines URT data as those available within 60 s post-satellite observation [19]. RT data, on the other hand, are available within 60 min, typically around 20–30 min, for the US and Canada. Once URT/RT data surpass 6 h in age, they are superseded by NRT data, which are globally accessible within 3 h of satellite observation [20].

The immediacy of URT/RT data is paramount for the early delineation of active fire perimeters, making it indispensable for operational use by fire management and firefighting agencies in Canada. This underscores the need for ongoing research to evaluate the efficacy of various algorithms, including combined approaches, for calculating forest fire perimeters. Such research is vital for enhancing rapid response capabilities and improving the overall effectiveness of fire management strategies.

While existing studies have explored forest fire perimeters using individual [16,21–26] or multiple algorithms [27], such as buffer [24–26], concave hull with an alfa shape [27], and convex hull algorithms [16,22,23], there remains a gap in comprehensive assessments. Notably, only a few studies have utilized both Moderate Resolution Imaging Spectroradiometer (MODIS) and Visible Infrared Imaging Radiometer Suite (VIIRS) active fire data [16,21,22], while a few studies have used single MODIS [24] or VIIRS [23,25,27]. The Canadian Wildland Fire Information System (CWFIS) relies on a combination of AVHRR, MODIS, and VIIRS data to generate daily active forest fire perimeters using the buffer algorithm [26]. However, most research, particularly outside the CWFIS framework, has been concentrated in the United States, often employing single algorithms rather than exploring the potential of multiple or combined algorithmic approaches.

Previous work by Briones-Herrera et al. [16] marked an initial foray into assessing forest fire perimeters for early mapping using NRT data and the convex hull algorithm, experimenting with various aggregation distances to understand their relationship with MODIS C6 burned area data (MCD64A1). Apart from those of the CWFIS, existing studies on assessing forest fire perimeters are mainly implemented in US regions. Conversely, all

these studies applied individual algorithms to delineate forest fire perimeters instead of evaluating multiple or combinations of multiple algorithms and satellites. Although one study applied the concave hull algorithm with several alfa values in California for assessing fire perimeters [27], other studies only used buffer round-shape approaches [24–26], while the buffer algorithm demonstrates both round and square shapes [28]. However, to the best of our knowledge, there is no comprehensive study that has used a multiple, or a combination of, algorithms approach with NRT or URT active fire data for delineating forest fire perimeters, particularly in Canada. Consequently, considering the increasing frequency and severity of forest fires in Canada, specifically in Alberta and the Northwest Territories [14], it is crucial to conduct more research for assessing the performance of individuals and multiple algorithms, including combination approaches to calculate forest fire perimeters with URT data.

This study is aimed at addressing the pressing need for accurate real-time fire monitoring by comparing the effectiveness of buffer, convex, and concave hull algorithms in estimating active fire perimeters. A comprehensive comparison is conducted to identify the most effective method for delineating forest fire boundaries, which is crucial for timely and effective fire management strategies. The performance of these algorithms, including their individual and combined applications, is evaluated using VIIRS Suomi National Polar-orbiting Partnership (SNPP) and MODIS active fire datasets from 2015 to 2021. To the best of our knowledge, this study is the first to assess active forest fire perimeters employing multiple algorithms in both standalone and integrated approaches, with a particular focus on the fires in Alberta and the Northwest Territories of Canada. The methodologies utilized here hold significant promise for future research endeavors aimed at enhancing the precision and promptness of forest fire perimeter assessments, leveraging NRT/URT active fire data to improve emergency response and mitigation efforts.

2. Study Area and Data Requirements

2.1. Study Region

The study area comprises the northern part of Alberta (AB) and the southern part of the Northwest Territories (NT), both characterized by extensive forested landscapes and diverse climatic conditions (see Figure 1). In this region, 30 forest fires were selected based on their size, ranging from very small to very large, occurring between 2015 and 2021. The majority of these fires occurred in Alberta, with fewer in the NT (see Figure 1). Remarkably, some fires extended across provincial boundaries into the NT, British Columbia (BC), and Saskatchewan (SK).

Geographically, Alberta is divided into 21 natural subregions within six regions, each characterized by distinctive landscape patterns, vegetation, soil types, elevations, and physiographic features, as organized by local climate, topography, and geology [6,17,29]. The province's elevation ranges from 150 to 3650 m above sea level, with an average annual rainfall of 510 mm and temperatures ranging from −7.1 to 6 °C. Alberta experiences long, cold winters and short summers [6]. This study examined fires occurring from April to October, each lasting from a single day to over a month. The affected areas varied, ranging from 200 to 500,000 hectares (Table 1 and Figure 1).

Table 1 provides a detailed account of significant wildfire events, including fire identification numbers, areas affected in hectares, dates of occurrence, responsible agencies, causes, and regions covered. Each entry included the fire number and its alias when available. The data spanned from 2015 to 2021, highlighting the impact and extent of wildfires across Alberta (AB) and neighboring regions, including the Northwest Territories (NT), British Columbia (BC), and Saskatchewan (SK). The causes of the fires were classified as follows: L for lightning-caused, U for unknown causes, and H for human-caused. The Horse River Fire, also known as the Fort McMurray Fire, was the most extensive event in 2016 [30], scorching over 490,000 hectares. Each fire was assigned a unique identifier based on the Alberta government's classification system [31,32]. While most fires were identified

by numbers, some had names designated by agencies like AB (Alberta), NT (Northwest Territories), and PC-WB (Wood Buffalo National Park).
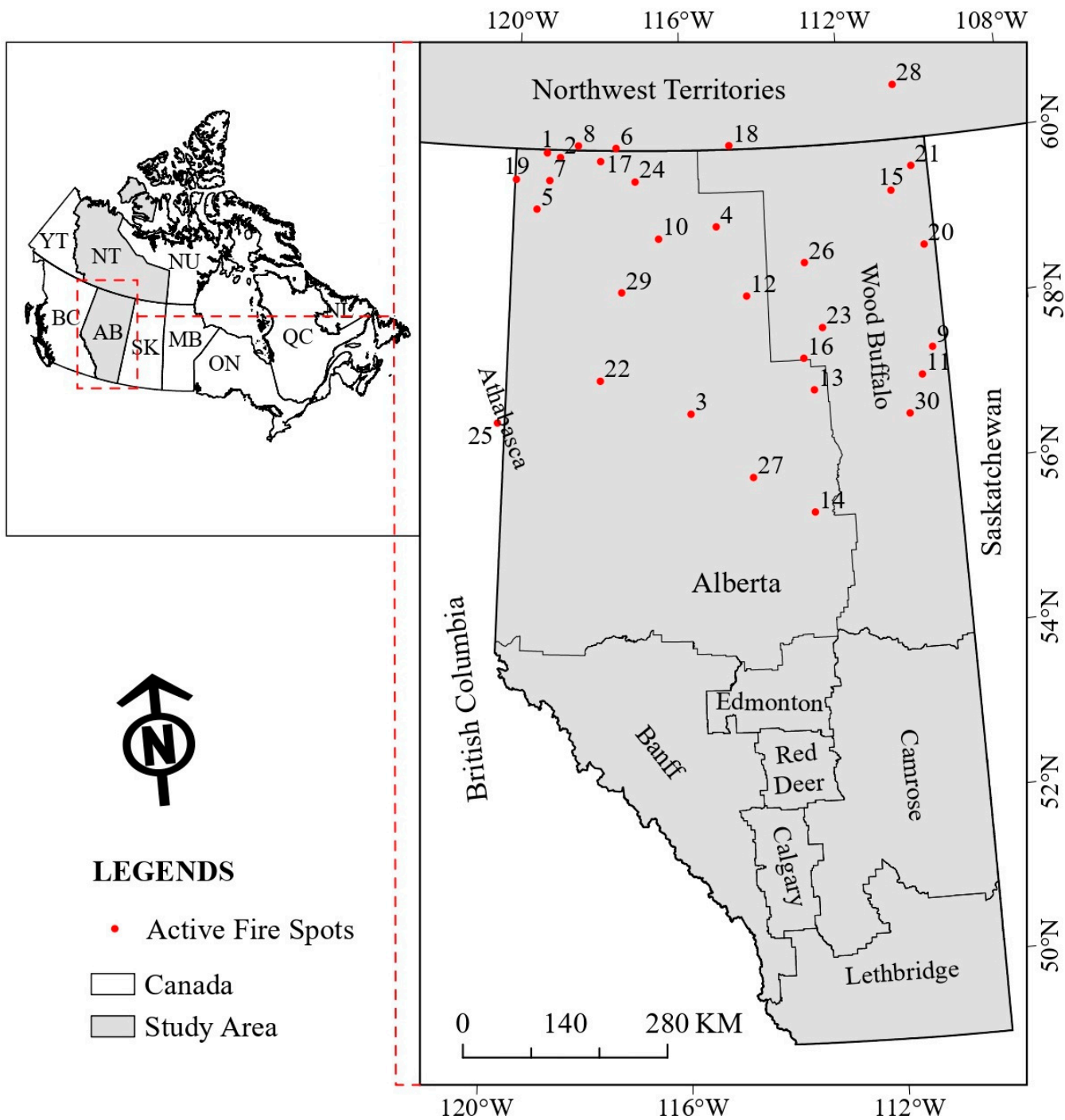

Figure 1. The study area includes 30 forest fires from the provinces of Alberta and the Northwest Territories in Canada. The details regarding these 30 forest fires are included in Table 1.

Table 1. Summary of major forest fires in Alberta and surrounding regions during the period 2015–2021. The table includes the following columns: fire number (unique ID), alias (common name, if available), area (ha) (area affected in hectares), start date, end date, agency (responsible managing agency, e.g., AB for Alberta, NT for Northwest Territories, and PC for Parks Canada), causes (L for lightning, U for unknown, and H for human), and covered (regions affected, e.g., AB for Alberta, NT for Northwest Territories, BC for British Columbia, and SK for Saskatchewan).

#	Fire Number	Alias	Area (ha)	Start Date	End Date	Agency	Causes	Covered
1	HWF-100-2016	*	229.66	10-Jun-16	10-Jun-16	AB	L	AB
2	HWF-193-2016	*	553.53	15-Jul-16	18-Jul-16	AB	U	AB
3	SWF-030-2016	*	1671.48	30-Apr-16	4-May-16	AB	L	AB
4	HWF-252-2017	*	1703.37	13-Aug-17	23-Aug-17	AB	L	AB
5	HWF-177-2018	*	2633.75	27-Jul-18	28-Jul-18	AB	L	AB
6	SS-021-2019	*	3045.57	21-Jul-19	25-Jul-19	AB	L	AB-NT
7	HWF-137-2018	*	3600.40	24-Jun-18	12-Jul-18	AB	L	AB
8	SS-010-2019	*	3715.39	15-Jun-19	17-Jun-19	NT	L	NT
9	MWF-079-2021	*	3263.49	14-Jul-21	13-Aug-21	AB	L	AB
10	HWF-083-2018	Little Rapids Fire	4117.34	24-May-18	28-May-18	AB	L	AB
11	MWF-059-2021	*	3605.36	13-Jul-21	15-Jul-21	AB	L	AB
12	HWF-221-2017	Moose Lake Complex Fire	4709.00	5-Aug-17	22-Aug-17	AB	L	AB
13	SWF-094-2018	Rabbit Lake Fire	5028.97	24-Jun-18	25-Jun-18	AB	L	AB
14	LWF-099-2018	Rock Island Complex Fire	7278.63	22-May-18	29-May-18	AB	L	AB
15	MWF-054-2019	Bocquene Complex Fire	8213.26	17-Jul-19	25-Jul-19	AB	L	AB
16	SWF-107-2017	Muskrat Lake Fire	12,729.14	14-Aug-17	8-Sep-17	AB	U	AB
17	HWF-280-2017	*	13,638.27	6-Sep-17	8-Sep-17	AB	L	AB
18	WB-039-2015	*	18,572.76	27-Jun-15	12-Aug-15	PC-WB	U	AB-NT
19	HBZ-001-2015	*	17,932.28	25-Jun-15	7-Jul-15	AB	L	AB-BC
20	MWF-051-2019	Old Fort Complex Fire	24,040.20	17-Jul-19	25-Jul-19	AB	L	AB
21	MWF-052-2015	*	22,356.65	24-Jun-15	13-Aug-15	AB	L	AB
22	PWF-052-2019	Battle Complex Fire	36,520.76	11-May-19	17-Jun-19	AB	U	AB
23	MWF-101-2015	*	57,674.08	27-Jun-15	28-Jul-15	AB	L	AB
24	HWF-066-2019	Jackpot Creek Fire	64,711.04	27-May-19	11-Jul-19	AB	U	AB
25	ABC-001-2016	Sweeney Creek Fire	72,527.47	18-Apr-16	29-Jul-16	AB	H	AB-BC
26	WB-004-2015	*	223,766.96	28-May-15	1-Oct-15	PC-WB	U	AB
27	SWF-049-2019	McMillan Complex Fire	222,869.05	18-May-19	21-Jul-19	AB	U	AB
28	SS-019-2017	*	269,583.55	7-Jul-17	19-Aug-17	NT	L	NT
29	HWF-042-2019	Chuckegg Creek Fire	335,032.56	12-May-19	13-Sep-19	AB	U	AB
30	MWF-009-2016	Horse River Wildfire	490,964.79	1-May-16	6-Aug-16	AB	U	AB-SK

* The official alias name for these fires is not available.

2.2. Datasets

2.2.1. Active Fire Data

This research utilized thermal anomaly data from two satellite sources: the VIIRS on the SNPP with a 375 m spatial resolution [33,34] and the MODIS (aqua and terra), which combines data from both the Terra and Aqua satellites [35,36]. Specifically, VIIRS (SNPP) I Band 375 m Active Fire Product NRT (VNP14IMGTDL_NRT) [34] and MODIS/Aqua + Terra Thermal Anomalies/Fire locations 1 km FIRMS V0061 NRT (MCD14DL-NRT v0061) were used [35]. These datasets are provided on an annual basis and are outputs of the Fire Information for Resource Management System (FIRMS) [37], an initiative started in 2007 by the University of Maryland. This initiative is supported by NASA's Applied Sciences Program and the United Nations Food and Agriculture Organization (UN FAO) [38].

The VIIRS and MODIS datasets provide near-real-time information on active fire locations and thermal anomalies, each offering a daily temporal resolution. The VIIRS SNPP satellite passes over the equator at approximately 13:30 MT (local time) and 01:30 MT, making two Earth observations per day. In contrast, the MODIS Terra satellite passes at about 10:30 MT and 22:30 MT, while the MODIS Aqua does so at 01:30 MT and 13:30 MT, resulting in at least four daily observations from the satellites. Although the potential for observations ranges from six to eight times daily, this study analyzed data from each

instrument separately within the specific period of each fire's duration. Meanwhile, the active fire data in CSV format, containing data points from these satellites, were utilized for the years 2015 to 2021 [39].

2.2.2. Reference Data

The research incorporated data from the National Burn Area Composite (NBAC), which is a GIS-based dataset spanning from 2015 to 2021 [40,41], to corroborate the Active Fire Perimeter (AFP) estimates. The NBAC is an integral component of the Fire Monitoring, Accounting, and Reporting System (FireMARS), created by Natural Resources Canada's (NRC's) Canada Centre for Mapping and Earth Observation (CCMEO) in conjunction with the Canadian Forest Service. This dataset aggregates annual maps of burned areas, drawing 81% of its information from 30 m resolution Landsat imagery [41], 10% from high-resolution images captured by aircraft and satellites with resolutions finer than 5 m, and the remaining 9% from comprehensive aerial surveys [42].

2.2.3. Land Cover Data

This study also utilized the MODIS Land Cover Type Yearly Global 500 m MODIS (MCD12Q1 v061) dataset [43], which is a global annual land use and land cover product with a 500 m spatial resolution [43]. This dataset was employed to exclude areas covered by water from the burn area perimeters calculated in the research [44].

3. Methods

A time series overlay was utilized to aggregate active fire data points, which were aligned with the individual start and end dates of fires, as detailed in Table 1. Data points from the VIIRS and MODIS annual datasets were extracted for 30 historical fires. These data points were then used to determine the individual fire boundaries, following the NBAC fire polygons shown in Figure 2. Clusters of data points within and around the NBAC polygons were identified as individual fires, and from these, 30 sets of aggregated data points were extracted for subsequent analysis. When multiple clusters of data points are detected within the region of interest (ROI), a subdivision strategy is proposed. The ROI is partitioned into smaller subregions, and each subregion is analyzed independently using the designated algorithm.

Active fire perimeter calculation algorithms, both individual and combined, were applied to the aggregated data points. MODIS-based annual land cover data were employed to exclude water-covered areas from the fire perimeters calculated. Following the calculation of the perimeters, error metrics such as commission and omission errors, as well as matching agreement, were computed to evaluate the accuracy of the algorithms utilized in this study. A brief overview of the forest fire perimeter algorithms is provided in this section.

3.1. Buffer, Concave, and Convex

A zone is created around spatial features (such as points, polylines, or polygons) at a specified distance by the buffer algorithm [45,46] in Geographic Information Systems (GIS). Two buffer shapes, round and square, are determined based on the spatial resolution of the active fire data: 375 m for VIIRS and 1000 m for MODIS. By default, buffer distances are calculated in grid units in QGIS, which necessitates reprojection [47,48]. Consequently, the active fire data were reprojected to NAD 1983 Albers Canada (ESRI: 102001) to enable the calculation of buffer distances in meters [47,48]. Both round and square buffer shapes were evaluated for 30 fires to ascertain the more effective shape for delineating fire perimeters.

The term concave hull was first introduced by Galton and Duckham in 2006 and further developed in 2007 [49]. The concave hull algorithm is utilized in various fields [50–53], including 3D modeling [51], GIS [52], and medicine [53]. The algorithm defines two main shapes: the alpha (α) shape algorithm and the k-nearest neighbors algorithm. The α-shape concave hull algorithm is based on [54] the Delaunay triangulation approach,

which involves cutting the edges of triangles to form a concave shape [50]. In contrast, the k-nearest neighbors algorithm operates by searching for the nearest points. This study employs the α-shape concave hull algorithm using the QGIS platform [50,55].
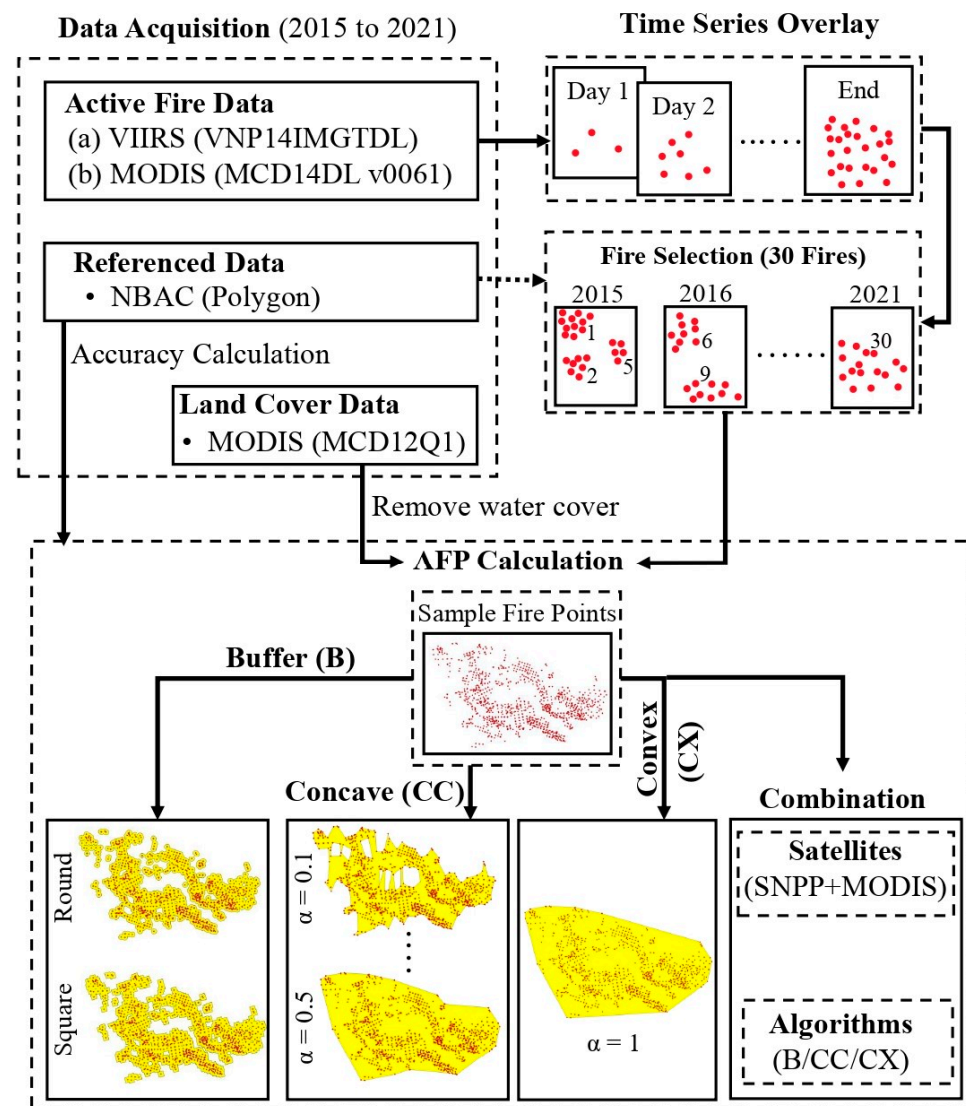

Figure 2. Workflow diagram of data acquisition and analysis for forest fire events (2015–2021). This diagram illustrates the systematic process from collecting active fire data using VIIRS and MODIS, through accuracy assessments with NBAC polygon data, to the final combination of satellite observations and algorithms for active fire perimeter (AFP) calculation.

In QGIS, the α-shape concave hull algorithm provides a threshold value range between 0 and 1. Values greater than 0.5 result in a less concave shape (with 1 being completely convex), while values less than 0.5 produce more concave shapes. Due to uncertainties in selecting the optimal α parameter, a series of values between 0.1 and 0.5 was tested for 30 fires in this study. The threshold parameter that yielded the best results was then used to calculate forest fire perimeters.

Furthermore, the computational algorithm for the convex hull, also known as Minimum Bounding Geometry, was first developed in 1972. An O $(n\log n)$ algorithm was created to compute the convex hull of n points in the plane [56]. Generally, the convex hull algorithm encloses the entire layer or group subsets of features (points) with a vector polygon [28] in a convex shape, similar to the concave hull algorithm. In the QGIS platform, this is represented by a threshold value of 1, derived from the concave hull threshold range.

3.2. Combination Approach

The combination approach involves merging (union-∪ combination) data from two satellites (MODIS and VIIRS) or algorithms (buffer-B, concave-CC, and convex-CX) into a single output for a particular fire event. This approach calculates forest fire perimeters by combining data such as the union of the VIIRS buffer and MODIS buffer (VIIRS-B ∪ MODIS-B), VIIRS buffer square and MODIS buffer square (VIIRS-Bsq ∪ MODIS-Bsq), VIIRS-CC ∪ MODIS-CC, and VIIRS-CX ∪ MODIS-CX. Additionally, the combination of algorithms follows similar merging (union-∪/dissolved) methods among each satellite's calculated algorithms, such as B ∪ CC, Bsq ∪ CC, B ∪ CX, and Bsq ∪ CX, respectively. A summary of the workflow used in this study is provided in Figure 2.

3.3. Accuracy Metrics

After water bodies were excluded from the AFP estimates, accuracy assessments were conducted. This study employed error metrics derived from the confusion matrix to evaluate spatial performance and accuracy: the commission error (CE) and omission error (OE), along with the matching metric, comparing the referenced burned area to the calculated AFP. The matching metric indicates the congruence between the calculated and referenced data.

$$\text{Matching} = \frac{\text{Total Intersect Area}}{\text{Total Referenced Area}} \times 100\%, \tag{1}$$

$$\text{Commission Error (CE)} = \frac{\text{Total Calculated Area} - \text{Total Intersect Area}}{\text{Total Calculated Area}} \times 100\%, \tag{2}$$

$$\text{Omission Error (OE)} = \frac{\text{Total Referenced Area} - \text{Total Intersect Area}}{\text{Total Referenced Area}} \times 100\%. \tag{3}$$

Here, the Total Intersect Area is the overlap between the referenced (NBAC) and calculated data (AFP), while the Total Calculated Area comes from the forest fire perimeter calculations for a specific fire. The Total Referenced Area is derived from NBAC data. It is important to note that the omission error can also be interpreted as

$$\text{Omission Error (OE)} = 100\% - \text{Matching} \tag{4}$$

Therefore, in the results section, the OE will not be provided to avoid redundancy.

4. Results

4.1. Comparative Analysis of Geospatial Error Detection

Figure 3 presents a comparison between two algorithms used for error detection in geographical data analysis: the concave hull algorithm and the buffer algorithm.

The concave hull algorithm, depicted on the left side of each map set, was designed to closely follow the contours of the data points, creating a concave boundary that wrapped tightly around a set of points. This method was particularly useful for identifying errors in sparse or irregularly distributed data, as it minimized the inclusion of empty space within the hull, leading to a more precise identification of commission errors (highlighted in yellow) and omission errors (highlighted in red).

On the other hand, the buffer algorithm, shown on the right side of each map set, created a buffer zone around the data points, effectively capturing areas that might have extended beyond the immediate vicinity of the points. This approach could be advantageous when dealing with dense or regularly distributed data, as it allows for a broader search area, potentially catching errors that the concave hull might have missed. However, it might also have included more matching areas (marked with diagonal lines), which did not contain errors but were within the buffer zone.

Each pair of maps (labeled a through d) demonstrated the algorithms' performance across different scenarios, with the complexity and density of errors increasing from map a to map d.
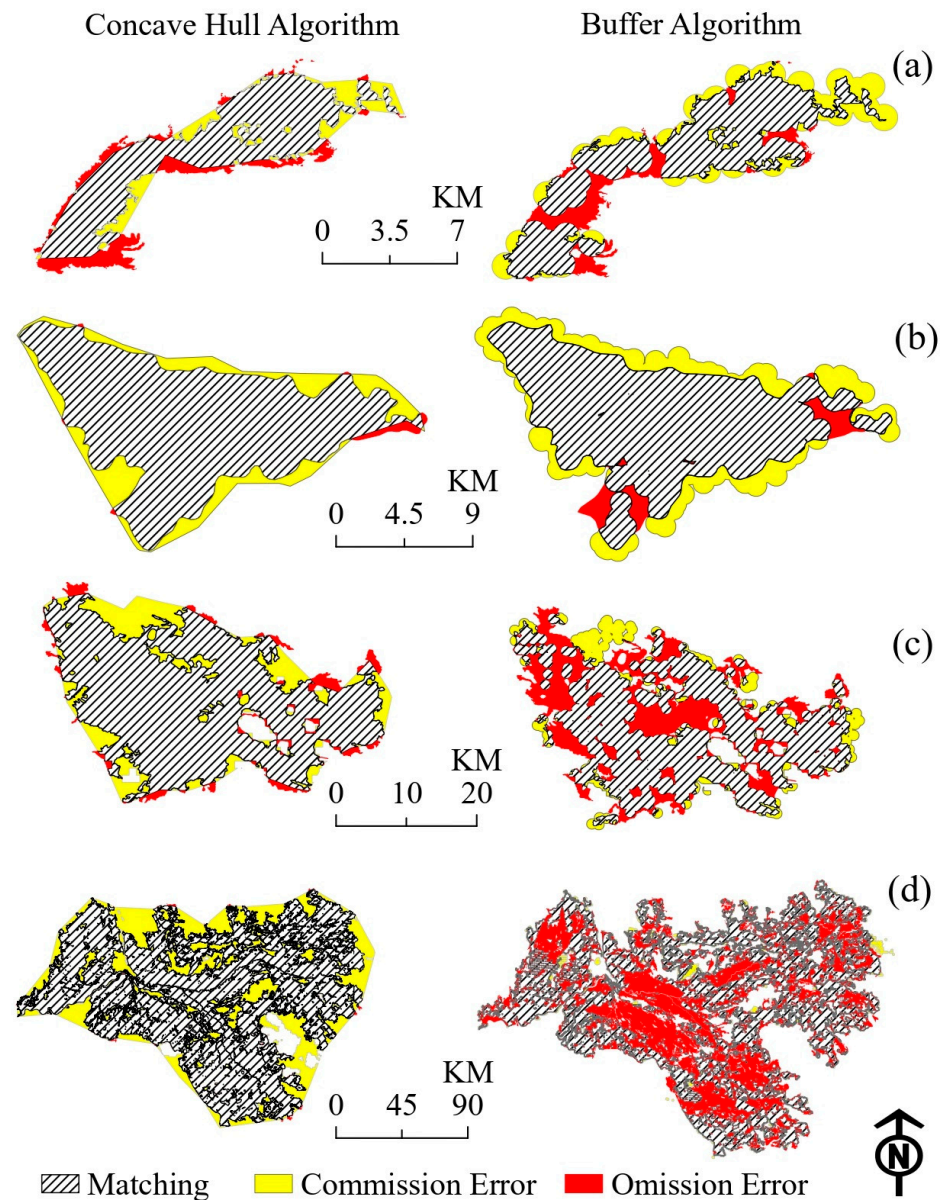
Concave Hull Algorithm   Buffer Algorithm

Figure 3. Comparative analysis of geospatial error detection: concave hull vs. buffer algorithms. The figure illustrates a side-by-side comparison of the concave hull algorithm and the buffer algorithm in identifying errors within geographical data. Four pairs of maps (those labeled (**a–d**) correspond to Table 1 and fires 3, 12, 18, and 30, respectively) showcase the effectiveness of each algorithm in detecting commission errors (yellow) and omission errors (red), with areas of agreement marked by diagonal lines.

4.2. Matching and Commission Error (CE) Percentages for VIIRS and MODIS Datasets

Table 2 presents matching and CE percentages for the VIIRS and MODIS datasets across different concave α values, ranging from 0.1 to 0.5. Matching indicates the percentage of the referenced area that intersects with the calculated area, reflecting how accurately the calculated area aligns with the referenced area. CE represents the percentage of the calculated area that does not intersect with the referenced area, indicating the extent of overestimation in the calculated area.

Table 2. Matching and commission error (CE) percentages for VIIRS and MODIS datasets across different concave α values. The table shows how the alignment of the calculated area with the referenced area (matching) and the overestimation of the calculated area (CE) vary as the α value increases from 0.1 to 0.5.

Concave (α Values)		0.1	0.2	0.3	0.4	0.5
VIIRS	Matching	68.91	77.77	81.14	82.71	84.06
	CE	20.59	24.60	27.33	29.71	31.64
MODIS	Matching	57.71	66.27	70.28	73.07	74.98
	CE	25.58	28.63	29.98	31.96	32.99

For the VIIRS dataset, as the concave α value increased from 0.1 to 0.5 and the matching percentage improved from 68.91% to 84.06%, indicating a better alignment of the calculated area with the referenced area. However, the CE also increased from 20.59% to 31.64%, showing a higher degree of overestimation. Similarly, for the MODIS dataset, the matching percentage improved from 57.71% to 74.98% as the α value increased, though it remained generally lower than that of the VIIRS dataset. The CE for the MODIS dataset also increased from 25.58% to 32.99%, reflecting a similar trend of increasing overestimation. Overall, the data indicated a trade-off, as the concave α values increased the alignment of the calculated area with the referenced area improved, but this also led to increased overestimation. This pattern was observed consistently in both the VIIRS and MODIS datasets.

Table 3 presents the comparison of different methods for sensor data matching and their corresponding CE using VIIRS, MODIS, and a combination of both sensors. The methods evaluated include buffer (B), buffer square (BSq), concave (CC), convex (CX), and combinations of these methods (B $\cup$ CC, BSq $\cup$ CC, B $\cup$ CX, BSq $\cup$ CX). The α value for the CC algorithms was selected by identifying those that provided a CE of less than 25% for VIIRS and less than 30% for MODIS. Therefore, an α value of 0.2 was used for VIIRS, and 0.3 for MODIS, due to the superior output in AFP calculation through the CC algorithm.

Table 3. Comparison of match percentages and commission errors (CE) for different methods using VIIRS, MODIS, and a combination of both sensors.

Sensors	VIIRS (%)		MODIS (%)		COMBINATION (%)	
Methods	**Match**	**CE**	**Match**	**CE**	**Match**	**CE**
Buffer (B)	75.11	24.56	81.99	40.52	89.65	40.12
Buffer Square (BSq)	78.56	26.31	85.24	42.95	91.56	42.71
Concave (CC)	77.77	24.60	70.28	29.98	83.19	30.25
Convex (CX)	87.60	36.09	81.23	37.54	89.86	39.68
B $\cup$ CC	86.33	29.55	87.69	42.74		
BSq $\cup$ CC	87.63	30.69	89.52	44.80		
B $\cup$ CX	91.24	38.33	91.05	46.90		
BSq $\cup$ CX	91.91	39.05	92.19	48.58		

For the VIIRS sensor, the buffer method achieved a match percentage of 75.11% with a CE of 24.56%, while buffer square improved the match to 78.56% and CE to 26.31%. The concave method had a match of 77.77% and a CE of 24.60%, whereas convex achieved a higher match of 87.60% and a CE of 36.09%. The combination methods showed that B $\cup$ CC had a match of 86.33% with a CE of 29.55%, BSq $\cup$ CC had an 87.63% match and 30.69% CE, B $\cup$ CX had a 91.24% match and 38.33% CE, and BSq $\cup$ CX had the highest match at 91.91% with a CE of 39.05%.

For the MODIS sensor, the buffer method achieved an 81.99% match with a CE of 40.52%, and buffer square further improved these values to 85.24% and 42.95%, respectively. The concave method showed a lower match of 70.28% with a CE of 29.98%, while convex showed a match of 81.23% with a CE of 37.54%. The combination methods demonstrated that B ∪ CC had a match of 87.69% with a CE of 42.74%, BSq ∪ CC had an 89.52% match and 44.8% CE, B ∪ CX had a 91.05% match and 46.90% CE, and BSq ∪ CX had the highest match of 92.19% with a CE of 48.58%.

Using a combination of both sensors, the buffer method achieved an 89.65% match with a CE of 40.12%, while buffer square showed improvements, with a 91.56% match and a CE of 42.71%. The concave method achieved an 83.19% match with a CE of 30.25%, and the convex method showed a match of 89.86% with a CE of 39.68%. Combination methods for both sensors were not presented in the table.

The combination of sensors generally improved the match percentages across different methods, indicating better performance compared to individual sensors. Among the individual methods, convex tended to perform better in terms of higher match percentages, although it might have resulted in higher commission errors. The buffer square method also showed consistent improvements in match percentages over the buffer method. Combining different methods (e.g., B ∪ CX and BSq ∪ CX) generally yielded the highest match percentages but might have come at the cost of increased commission errors.

5. Discussion

The trade-off between matching and CE percentages was highlighted when analyzing different concave α values within the VIIRS and MODIS datasets. As the concave α value increased, the alignment of the calculated area with the referenced area improved, as evidenced by higher matching percentages. However, this improvement was accompanied by an increase in CE, indicating greater overestimation. This trend was consistent across both datasets, with the VIIRS dataset generally exhibiting higher matching percentages than the MODIS dataset. The observed trade-off suggested that while higher concave α values might enhance alignment accuracy, they also increased the risk of overestimating the error regions.

In Table 3, the comparison of different methods for sensor data matching and their corresponding CEs using VIIRS, MODIS, and a combination of both sensors provided additional insights. The buffer and buffer square methods consistently showed high matching percentages but also high CEs, reflecting their propensity for overestimation. The concave method demonstrated a more balanced approach with moderate matching percentages and a lower CE, indicating better precision in error detection. The convex method, although achieving the highest matching percentages, incurred significant overestimations, suggesting its suitability for scenarios where exhaustive error detection was prioritized over precision.

The combination methods (e.g., B ∪ CC, BSq ∪ CC, B ∪ CX, and BSq ∪ CX) generally yielded the highest match percentages but also came with increased commission errors. This finding underscored the potential benefit of combining different methods to enhance overall performance, particularly in complex or heterogeneous datasets. The combination of sensors typically improved match percentages, indicating better performances compared to using individual sensors. This enhancement suggested that integrating multiple data sources could provide a more comprehensive and accurate geospatial error detection framework.

Overall, the results highlighted the importance of context-specific algorithm selection in geospatial error detection. The choice between precision (concave hull) and comprehensiveness (buffer) depended on the data distribution and the specific requirements of the analysis. The trade-offs between matching accuracy and overestimation had to be carefully considered to optimize error detection performance. Future research could explore hybrid approaches that dynamically adjust the balance between precision and comprehensiveness based on real-time data characteristics, potentially mitigating the limitations observed in this study. Additionally, the integration of more diverse datasets and advanced machine

learning techniques could further enhance the robustness and accuracy of geospatial error detection methodologies.

This study utilized NRT active fire data; however, the initial objectives and methodology were tailored for URT data. At present, URT active fire data with global coverage is scarce, with the majority being confined to the USA and Canada [19]. Consequently, the focus of this study was narrowed to Canada, rather than adopting a global viewpoint. Despite this, the methodology developed in this study holds potential for broader geographical applications and would be enhanced by preliminary testing in diverse regions.

6. Concluding Remarks

This study presented a detailed comparative analysis of the concave hull and buffer algorithms for the estimation of active fire perimeters, elucidating their respective strengths and limitations. The concave hull algorithm demonstrated higher precision in identifying commission and omission errors, particularly in sparse or irregularly distributed datasets. In contrast, the buffer algorithm excelled in detecting errors within dense or regularly distributed data by encompassing a broader search area, albeit with a tendency towards overestimation.

The investigation into matching and commission error (CE) percentages for the VIIRS and MODIS datasets revealed a consistent trade-off: increasing the concave α value enhanced the alignment of the calculated area with the referenced area, but also raised the risk of overestimation. This pattern underscored the importance of context-specific algorithm selection based on the characteristics of the geospatial data and the specific requirements of the error detection task.

Further, the comparative analysis of different methods for sensor data matching using VIIRS, MODIS, and their combination indicated that while methods like buffer and buffer square achieved high matching percentages, they also incurred higher commission errors. The concave method offered a balanced approach, with moderate matching percentages and lower CEs, while the convex method, despite its highest matching percentages, suffered from significant overestimation. Combining different methods and sensors generally improved match percentages, suggesting that integrated approaches could enhance overall performance in complex datasets.

In conclusion, this study highlighted the critical need for careful algorithm selection in geospatial error detection, balancing precision and comprehensiveness based on data distribution and analytical goals. Future research should focus on developing hybrid approaches that adaptively balance these trade-offs, integrating advanced machine learning techniques and diverse datasets to improve the robustness and accuracy of geospatial error detection methodologies. This approach would provide a more effective framework for researchers and practitioners in the field of geospatial analysis, enabling more accurate and reliable error detection in various applications.

Our study conducts a thorough evaluation of Canada's burned areas, utilizing the Fire Information for Resource Management System (FIRMS) for its near-real-time data capabilities. While such data are available on a global scale, our research is tailored to harness ultra real-time data, a resource presently limited to the United States and Canada. This strategic decision is in line with our commitment to delivering the most immediate and precise wildfire assessments. Anticipating future developments, we have designed our study to be flexible and scalable, ready to incorporate ultra real-time data from other regions as it becomes globally accessible.

Author Contributions: Conceptualization, H.B., H.D. and Q.K.H.; methodology, H.B., H.D. and Q.K.H.; formal analysis, H.B. and Q.K.H.; writing—original draft preparation, H.B.; writing—review and editing, H.D., M.R.A. and Q.K.H.; supervision, Q.K.H.; funding acquisition, Q.K.H. All authors have read and agreed to the published version of the manuscript.

Abbreviations

The following abbreviations are used in this manuscript:

AFP	Active fire perimeter
AVHRR	Advanced very high-resolution radiometer
B	Buffer
CAD	Canadian dollar
CC	Concave hull algorithm
CCMEO	Canada Centre for Mapping and Earth Observation
CE	Commission error
CIFFC	Canadian Interagency Forest Fire Centre
CWFIS	Canadian Wildland Fire Information System
CX	Convex hull algorithm
EOSDIS	Earth Observing System Data and Information System
FAO	Food and Agriculture Organization
FireMARS	Fire Monitoring, Accounting, and Reporting System
FIRMS	Fire Information for Resource Management System
GIS	Geographic Information System
Mha	Million hectares
MODIS	Moderate Resolution Imaging Spectroradiometer
MT	Mountain Time
NAD	North American Datum
NASA	National Aeronautics and Space Administration's
NBAC	National Burn Area Composite
NRC	Natural Resources Canada
NRT	Near-real-time
NT	Northwest Territories
OE	Omission error
RT	Real-Time
SNPP	Suomi National Polar-orbiting Partnership
UN	United Nations
URT	Ultra-real-time
VIIRS	Visible Infrared Imaging Radiometer Suite

References

1. Tyukavina, A.; Potapov, P.; Hansen, M.C.; Pickens, A.H.; Stehman, S.V.; Turubanova, S.; Parker, D.; Zalles, V.; Lima, A.; Kommareddy, I.; et al. Global Trends of Forest Loss Due to Fire From 2001 to 2019. *Front. Remote Sens.* **2022**, *3*, 825190. [CrossRef]
2. Giglio, L.; Boschetti, L.; Roy, D.P.; Humber, M.L.; Justice, C.O. The Collection 6 MODIS Burned Area Mapping Algorithm and Product. *Remote Sens. Environ.* **2018**, *217*, 72–85. [CrossRef] [PubMed]
3. Dastour, H.; Hassan, Q.K. Utilizing MODIS Remote Sensing and Integrated Data for Forest Fire Spread Modeling in the Southwest Region of Canada. *Environ. Res. Commun.* **2024**, *6*, 025007. [CrossRef]
4. Saleh, A.; Zulkifley, M.A.; Harun, H.H.; Gaudreault, F.; Davison, I.; Spraggon, M. Forest Fire Surveillance Systems: A Review of Deep Learning Methods. *Heliyon* **2024**, *10*, e23127. [CrossRef] [PubMed]
5. Arteaga, B.; Diaz, M.; Jojoa, M. Deep Learning Applied to Forest Fire Detection. In Proceedings of the 2020 IEEE International Symposium on Signal Processing and Information Technology (ISSPIT), Louisville, KY, USA, 9–11 December 2020; pp. 1–6.
6. Ahmed, M.R.; Hassan, Q.K. Occurrence, Area Burned, and Seasonality Trends of Forest Fires in the Natural Subregions of Alberta over 1959–2021. *Fire* **2023**, *6*, 96. [CrossRef]

7. Dastour, H.; Ahmed, M.R.; Hassan, Q.K. Analysis of Forest Fire Patterns and Their Relationship with Climate Variables in Alberta's Natural Subregions. *Ecol. Inform.* **2024**, *80*, 102531. [CrossRef]
8. Chatenoux, B.; Peduzzi, P. *Biomass Fires: Preliminary Estimation of Ecosystems Global Economic Losses*; UNEP/GRID-Geneva: Geneva, Switzerland, 2012.
9. Page, S.E.; Siegert, F.; Rieley, J.O.; Boehm, H.-D.V.; Jaya, A.; Limin, S. The Amount of Carbon Released from Peat and Forest Fires in Indonesia during 1997. *Nature* **2002**, *420*, 61–65. [CrossRef]
10. Stefanidou, M.; Athanaselis, S.; Spiliopoulou, C. Health Impacts of Fire Smoke Inhalation. *Inhal. Toxicol.* **2008**, *20*, 761–766. [CrossRef] [PubMed]
11. Kales, S.N.; Soteriades, E.S.; Christophi, C.A.; Christiani, D.C. Emergency Duties and Deaths from Heart Disease among Firefighters in the United States. *N. Engl. J. Med.* **2007**, *356*, 1207–1215. [CrossRef]
12. Government of Alberta. *Flat Top Complex Wildfire Review Committee Flat Top Complex, Submitted to the Minister of Alberta Environment and Sustainable Resource Development*; Government of Alberta: Edmonton, AB, Canada, 2012; pp. 1–83.
13. Ahmed, M.; Hassan, Q.; Abdollahi, M.; Gupta, A. Introducing a New Remote Sensing-Based Model for Forecasting Forest Fire Danger Conditions at a Four-Day Scale. *Remote Sens.* **2019**, *11*, 2101. [CrossRef]
14. CIFFC. *Canada Report: 2023 Fire Season*; Canadian Interagency Forest Fire Centre: Winnipeg, MB, Canada, 2024.
15. Ban, Y.; Zhang, P.; Nascetti, A.; Bevington, A.R.; Wulder, M.A. Near Real-Time Wildfire Progression Monitoring with Sentinel-1 SAR Time Series and Deep Learning. *Sci. Rep.* **2020**, *10*, 1322. [CrossRef] [PubMed]
16. Briones-Herrera, C.I.; Vega-Nieva, D.J.; Monjarás-Vega, N.A.; Briseño-Reyes, J.; López-Serrano, P.M.; Corral-Rivas, J.J.; Alvarado-Celestino, E.; Arellano-Pérez, S.; Álvarez-González, J.G.; Ruiz-González, A.D.; et al. Near Real-Time Automated Early Mapping of the Perimeter of Large Forest Fires from the Aggregation of VIIRS and MODIS Active Fires in Mexico. *Remote Sens.* **2020**, *12*, 2061. [CrossRef]
17. Chuvieco, E.; Mouillot, F.; van der Werf, G.R.; San Miguel, J.; Tanase, M.; Koutsias, N.; García, M.; Yebra, M.; Padilla, M.; Gitas, I.; et al. Historical Background and Current Developments for Mapping Burned Area from Satellite Earth Observation. *Remote Sens. Environ.* **2019**, *225*, 45–64. [CrossRef]
18. Çolak, E.; Sunar, F. The Importance of Ground-Truth and Crowdsourcing Data for the Statistical and Spatial Analyses of the NASA FIRMS Active Fires in the Mediterranean Turkish Forests. *Remote Sens. Appl. Soc. Environ.* **2020**, *19*, 100327. [CrossRef]
19. Smith, J.M. *FIRMS Adds Ultra Real-Time Data from MODIS and VIIRS | Earthdata*; NASA: Washington, DC, USA, 2022.
20. Davies, D. Wildfire Detection in the US and Canada within a Minute of Satellite Observation. Available online: https://wiki.earthdata.nasa.gov/display/FIRMS/2022/07/14/Wildfire+detection+in+the+US+and+Canada+within+a+minute+of+satellite+observation (accessed on 21 May 2024).
21. Briones-Herrera, C.I.; Vega-Nieva, D.J.; Briseño-Reyes, J.; Monjarás-Vega, N.A.; López-Serrano, P.M.; Corral-Rivas, J.J.; Alvarado, E.; Arellano-Pérez, S.; Jardel Peláez, E.J.; Pérez Salicrup, D.R.; et al. Fuel-Specific Aggregation of Active Fire Detections for Rapid Mapping of Forest Fire Perimeters in Mexico. *Forests* **2022**, *13*, 124. [CrossRef]
22. Artés, T.; Boca, R.; Liberta, G.; San-Miguel, J. Non-Supervised Method for Early Forest Fire Detection and Rapid Mapping. In Proceedings of the Fifth International Conference on Remote Sensing and Geoinformation of the Environment (RSCy2017), Paphos, Cyprus, 20–23 March 2017; SPIE: Bellingham, WA, USA, 2017; Volume 10444, pp. 224–233.
23. Cardil, A.; Monedero, S.; Ramírez, J.; Silva, C.A. Assessing and Reinitializing Wildland Fire Simulations through Satellite Active Fire Data. *J. Environ. Manag.* **2019**, *231*, 996–1003. [CrossRef] [PubMed]
24. Henderson, S.B.; Ichoku, C.; Burkholder, B.J.; Brauer, M.; Jackson, P.L. The Validity and Utility of MODIS Data for Simple Estimation of Area Burned and Aerosols Emitted by Wildfire Events. *Int. J. Wildland Fire* **2010**, *19*, 844–852. [CrossRef]
25. Oliva, P.; Schroeder, W. Assessment of VIIRS 375m Active Fire Detection Product for Direct Burned Area Mapping. *Remote Sens. Environ.* **2015**, *160*, 144–155. [CrossRef]
26. Canadian Forest Service; Canadian Wildland Fire Information System (CWFIS); Natural Resources Canada; Canadian Forest Service; Northern Forestry Centre. *Fire M3 Season-to-Date Buffered Hotspots—Fire Perimeter Estimates 2022*; Canadian Wildland Fire Information System: Edmonton, AB, Canada, 2022.
27. Chen, Y.; Hantson, S.; Andela, N.; Coffield, S.R.; Graff, C.A.; Morton, D.C.; Ott, L.E.; Foufoula-Georgiou, E.; Smyth, P.; Goulden, M.L.; et al. California Wildfire Spread Derived Using VIIRS Satellite Observations and an Object-Based Tracking System. *Sci. Data* **2022**, *9*, 249. [CrossRef]
28. Menke, K.; Corti, P.; Smith, R., Jr.; Pirelli, L.; Van Hoesen, J. *Mastering QGIS*, 2nd ed.; Packt Publishing Ltd.: Birmingham, UK, 2016; ISBN 978-1-78646-362-3.
29. Dastour, H.; Hassan, Q.K. Quantifying the Influence of Climate Variables on Vegetation Through Remote Sensing and Multi-Dimensional Data Analysis. *Earth Syst. Environ.* **2024**, *8*, 165–180. [CrossRef]
30. Hassan, Q.K.; Rahaman, K.R.; Ahmed, M.R.; Hossain, S.M. Examining Post-Fire Perceptions of Selected Mitigation Strategies after the 2016 Horse River Wildland Fire in Alberta, Canada. *Appl. Sci.* **2021**, *11*, 10155. [CrossRef]
31. Delisle, G.P.; Hall, R.J. *Forest Fire History Maps of Alberta, 1931 to 1983*; Northern Forestry Centre, Canadian Forestry Service: Edmonton, AB, Canada, 1987; ISBN 0-662-15280-8.
32. Government of Alberta. *Fire Perimeter Data Standard*; Agriculture and Forestry: Edmonton, AB, Canada, 2017.
33. Schroeder, W.; Oliva, P.; Giglio, L.; Csiszar, I.A. The New VIIRS 375 m Active Fire Detection Data Product: Algorithm Description and Initial Assessment. *Remote Sens. Environ.* **2014**, *143*, 85–96. [CrossRef]

34. Giglio, L. *VIIRS/NPP Active Fires 6-Min L2 Swath 375m V002*; NASA EOSDIS Land Processes Distributed Active Archive Center: Sioux Falls, SD, USA, 2024.
35. Giglio, L.; Justice, C. *MODIS/Terra Thermal Anomalies/Fire 5-Min L2 Swath 1km V061*; NASA EOSDIS Land Processes DAAC: Sioux Falls, SD, USA, 2021.
36. Neves, A.K.; Pereira, J.M.C.; Silva, J.M.N.; Catarino, S.; Oliva, P.; Chuvieco, E.; Campagnolo, M.L. Active Fire-Based Dating Accuracy for Landsat Burned Area Maps Is High in Boreal and Mediterranean Biomes and Low in Grasslands and Savannas. *ISPRS J. Photogramm. Remote Sens.* **2024**, *209*, 461–471. [CrossRef]
37. Jiao, L.; Bo, Y. Near Real-Time Mapping of Burned Area by Synergizing Multiple Satellites Remote-Sensing Data. *GISci. Remote Sens.* **2022**, *59*, 1956–1977. [CrossRef]
38. Davies, D.K.; Ilavajhala, S.; Wong, M.M.; Justice, C.O. Fire Information for Resource Management System: Archiving and Distributing MODIS Active Fire Data. *IEEE Trans. Geosci. Remote Sens.* **2009**, *47*, 72–79. [CrossRef]
39. NASA-FIRMS. Providing Active Fire Data for Near-Real Time Monitoring and Applications. Available online: https://firms.modaps.eosdis.nasa.gov/map/ (accessed on 17 May 2024).
40. Hall, R.J.; Skakun, R.S.; Metsaranta, J.M.; Landry, R.; Fraser, R.H.; Raymond, D.; Gartrell, M.; Decker, V.; Little, J. Generating Annual Estimates of Forest Fire Disturbance in Canada: The National Burned Area Composite. *Int. J. Wildland Fire* **2020**, *29*, 878–891. [CrossRef]
41. Wang, X.; Oliver, J.; Swystun, T.; Hanes, C.C.; Erni, S.; Flannigan, M.D. Critical Fire Weather Conditions during Active Fire Spread Days in Canada. *Sci. Total Environ.* **2023**, *869*, 161831. [CrossRef] [PubMed]
42. Skakun, R.; Castilla, G.; Metsaranta, J.; Whitman, E.; Rodrigue, S.; Little, J.; Groenewegen, K.; Coyle, M. Extending the National Burned Area Composite Time Series of Wildfires in Canada. *Remote Sens.* **2022**, *14*, 3050. [CrossRef]
43. Sulla-Menashe, D.; Gray, J.M.; Abercrombie, S.P.; Friedl, M.A. Hierarchical Mapping of Annual Global Land Cover 2001 to Present: The MODIS Collection 6 Land Cover Product. *Remote Sens. Environ.* **2019**, *222*, 183–194. [CrossRef]
44. Li, L.; Zhan, W.; Ju, W.; Peñuelas, J.; Zhu, Z.; Peng, S.; Zhu, X.; Liu, Z.; Zhou, Y.; Li, J.; et al. Competition between Biogeochemical Drivers and Land-Cover Changes Determines Urban Greening or Browning. *Remote Sens. Environ.* **2023**, *287*, 113481. [CrossRef]
45. Bhatia, S.; Vira, V.; Choksi, D.; Venkatachalam, P. An Algorithm for Generating Geometric Buffers for Vector Feature Layers. *Geo-Spat. Inf. Sci.* **2013**, *16*, 130–138. [CrossRef]
46. Žalik, B.; Zadravec, M.; Clapworthy, G.J. Construction of a Non-Symmetric Geometric Buffer from a Set of Line Segments. *Comput. Geosci.* **2003**, *29*, 53–63. [CrossRef]
47. Ramdani, F. *Exploring the Earth with QGIS: A Guide to Using Satellite Imagery at Its Full Potential*; Springer Remote Sensing/Photogrammetry; Springer Nature: Cham, Switzerland, 2023; ISBN 978-3-031-46041-8.
48. De Lange, N. *Geoinformatics in Theory and Practice: An Integrated Approach to Geoinformation Systems, Remote Sensing and Digital Image Processing*; Springer Textbooks in Earth Sciences, Geography and Environment; Springer: Berlin/Heidelberg, Germany, 2023; ISBN 978-3-662-65757-7.
49. Moreira, A.; Santos, M. Concave Hull: A k-Nearest Neighbours Approach for the Computation of the Region Occupied by a Set of Points. In Proceedings of the Second International Conference on Computer Graphics Theory and Applications (GRAPP 2007), Barcelona, Spain, 8–11 March 2007; pp. 61–68.
50. Kalinina, D.; Ingilevich, V.; Lantseva, A.; Ivanov, S. Computing Concave Hull with Closed Curve Smoothing: Performance, Concaveness Measure and Applications. *Procedia Comput. Sci.* **2018**, *136*, 479–488. [CrossRef]
51. Wu, C.; Yuan, Y.; Tang, Y.; Tian, B. Application of Terrestrial Laser Scanning (TLS) in the Architecture, Engineering and Construction (AEC) Industry. *Sensors* **2021**, *22*, 265. [CrossRef] [PubMed]
52. Qin, R.; Lin, L.; Kuang, C.; Su, T.-C.; Mao, X.; Zhou, Y. A GIS-Based Software for Forecasting Pollutant Drift on Coastal Water Surfaces Using Fractional Brownian Motion: A Case Study on Red Tide Drift. *Environ. Model. Softw.* **2017**, *92*, 252–260. [CrossRef]
53. Soltaninejad, S.; Cheng, I.; Basu, A. Robust Lung Segmentation Combining Adaptive Concave Hulls with Active Contours. In Proceedings of the 2016 IEEE International Conference on Systems, Man, and Cybernetics (SMC), Budapest, Hungary, 9–12 October 2016; pp. 004775–004780.
54. Melkemi, M.; Djebali, M. Computing the Shape of a Planar Points Set. *Pattern Recognit.* **2000**, *33*, 1423–1436. [CrossRef]
55. Park, J.-S.; Oh, S.-J. A New Concave Hull Algorithm and Concaveness Measure for N-Dimensional Datasets. *Ournal Inf. Sci. Eng.* **2012**, *28*, 587–600.
56. Graham, R.L. An Efficient Algorith for Determining the Convex Hull of a Finite Planar Set. *Inf. Process. Lett.* **1972**, *1*, 132–133. [CrossRef]